PHYSICAL REVIEW B **108**, 184420 (2023)

Phase diagrams for magnetic field and temperature induced ferromagnetism in antiferromagnetic FeRh

A. G. Buzdakov,[1] I. A. Dolgikh,[2,3] K. A. Zvezdin,[4] A. K. Zvezdin,[5,6] K. Rubi,[2,3,*] U. Zeitler,[2,3] P. C. M. Christianen,[2,3]
Th. Rasing,[2] S. K. K. Patel,[7] R. Medapalli,[7] E. E. Fullerton,[7] E. T. Dilmieva,[3] and A. V. Kimel[2]
[1]*Interactive Fully Electrical Vehicles Srl, 10040 La Loggia TO, Italy*
[2]*Institute for Molecules and Materials, Radboud University, 6525 AJ Nijmegen, The Netherlands*
[3]*High Field Magnet Laboratory (HFML - EMFL), Radboud University, Toernooiveld 7, 6525 ED Nijmegen, The Netherlands*
[4]*Instituto P.M. Srl, 10138 Turin, Italy*
[5]*The Lebedev Physical Institute of the Russian Academy of Sciences, 119991 Moscow, Russia*
[6]*New Spintronic Technologies Ltd., 121205 Moscow, Russia*
[7]*Center for Memory and Recording Research, University of California San Diego, La Jolla, California 92093-0401, USA*

(Received 14 June 2023; revised 28 October 2023; accepted 31 October 2023; published 21 November 2023)

Both temperature (T) increase and/or application of an external magnetic field (H) are able to induce ferromagnetism in otherwise antiferromagnetic FeRh. We present a theory that allows us to predict H-T phase diagrams for FeRh, with a special emphasis on the canted antiferromagnetic phase. Both cases of in-plane and out-of-plane magnetic anisotropy in FeRh films are studied numerically, and the results of the simulations are compared with the results obtained via magneto-transport studies done in magnetic fields up to 34 T and x-ray magnetic circular dichroism measured at the Rh $L_{2,3}$ and Fe K absorption edges in magnetic fields up to 17 T. The comparisons suggest examples of the simulated H-T phase diagrams that are most suitable to fit the case of FeRh.

DOI: 10.1103/PhysRevB.108.184420

I. INTRODUCTION

Antiferromagnets [1,2] represent the largest, but the least explored class of magnetic materials. Recently, it has been realized that antiferromagnets can facilitate solutions for the fastest and most energy efficient spintronics, magnonics, and data storage technologies [3–5]. This potential has further boosted the fundamental interest in antiferromagnets and initiated the rapidly growing and booming fields of antiferromagnetic spintronics and altermagnetism [6,7].

FeRh was first discovered in 1938 [8] and from that time it was known as a material with a counterintuitive emergence of spontaneous magnetization upon heating (see Fig. 1). It is an outstanding antiferromagnet that can become ferromagnetic upon a temperature increase, applied strain, or magnetic field. More particularly, if without any magnetic field or strain the temperature of the material crosses the critical value of around 370 K, along with the magnetic changes, FeRh experiences an expansion of its unit cell by ≈1% [9], while its crystal structure (CsCl) remains the same [10]. The lattice expansion is accompanied by a sudden change of electric conductivity [11–15]. Below 370 K, Fe ions with a magnetic moment of about $3\mu_B$ are coupled antiferromagnetically, while above this temperature the alignment becomes ferromagnetic. Moreover, in the antiferromagnetic phase Rh has no magnetic moment, whereas upon the phase transition, Rh acquires a net magnetic moment of around $1\mu_B$ [16–18]. Nevertheless, the mechanism governing the heat-induced phase transition in FeRh has been a subject of intense debates for many decades.

After the discovery of antiferromagnetism in FeRh, it was realized that this heat-induced ferromagnetism must be interpreted as a first-order phase transition from a low-temperature antiferromagnetic (AFM) to a high-temperature ferromagnetic (FM) state. The first theoretical attempt to explain this phase transition dates back to 1960, when it was proposed that this is, in fact, a structural phase transition with a volume change [19]. The latter results in a change of interatomic distances, naturally leading to a change of sign in the exchange integrals and hence to a change of the order from an antiferro- to a ferromagnetic one. However, soon it was argued that the total change of entropy in this case is much larger than the change of the entropy of the lattice [20,21]. Hence the mechanism of the magneto-structural transition remained an open question.

The recent development of computational physics has revived the interests in this phase transition in FeRh and its material properties have become a subject of atomistic and *ab initio* simulations [22–28]. It is remarkable, however, that despite the numerous attempts, the H-T phase diagram, which is practically the cornerstone in understanding any magnetic phase transition, has not yet been explored theoretically for FeRh. Moreover, although it is absolutely clear that an external magnetic field can induce spin canting, such a state has not been reported for FeRh.

Here we develop a theory to predict H-T phase diagrams for FeRh with a special attention to the canted AFM phase. Using experimental data on electrical resistance in magnetic

---

[*] Present address: National High Magnetic Field Laboratory, Los Alamos National Laboratory, Los Alamos, New Mexico 875455, USA.

fields up to 34 T and XMCD at the Rh and Fe absorption edges in magnetic fields up to 17 T, we propose phase diagrams which fit the experimental data in the best way.

The paper is organized as follows: Section II explains the ingredients of the proposed mean-field model for FeRh. In Sec. III we describe the experimental data on electrical resistance of FeRh in high magnetic fields and reveal how the critical temperature of the first-order phase transition depends on the applied magnetic field. The data are further used as a reference to evaluate the validity of the calculated H-T phase diagrams. Section IV describes the results of the XMCD measurements and discusses which of the calculated H-T phase diagram fits the experimental data in the best way. Section V provides conclusions and summarizes the open questions.

II. MEAN-FIELD MODEL OF TEMPERATURE INDUCED FERROMAGNETISM IN ANTIFERROMAGNETIC FeRh

A. Thermodynamic potential

We describe the magnetic structure of FeRh in terms of three macrospin parameters: $\mathbf{M}_1$ and $\mathbf{M}_2$ are the magnetizations of the two antiferromagnetically coupled Fe sublattices, and $\mathbf{M}_{\mathrm{Rh}}$ is the magnetization of the Rh ions. The Rh-Rh exchange interaction is essentially zero and can be neglected, and the Rh ions are thus modeled as a paramagnet in the effective magnetic field generated by the net magnetization of the Fe ions $\mathbf{M} = \mathbf{M}_1 + \mathbf{M}_2$ and the strength of external magnetic field $\mathbf{H}$.

Hence, the free energy F of FeRh contains terms that represent (a) the exchange interaction between the Fe sublattices ($W_{\text{Fe-Fe}}$); (b) the energy corresponding to interaction between the spins of Rh and the effective magnetic field acting on them (W_{Rh}); (c) the interaction of the Fe spins with the external magnetic field and (d) the magnetic anisotropy experienced by the spins of Fe (W_{ani}). The magnetic anisotropy for the Rh spins is neglected. Finally, in order to reflect the magnetostructural changes in FeRh we also include a magnetostrictive term W_{MS}, resulting in

$$F = W_{\text{Fe-Fe}} + W_{\mathrm{Rh}} - \mu_0(\mathbf{M}_1 + \mathbf{M}_2)\cdot\mathbf{H} + W_{ani} + W_{MS}. \quad (1)$$

For the Fe-Fe term we use simple isotropic exchange $J_{ex}(\mathbf{M}_1 \cdot \mathbf{M}_2)$, but for consistency we assume that $J_{ex} \propto 1/\chi_{\mathrm{Fe}}$ [29], and in order to account for the energy per one ion we include a factor of two in the denominator:

$$W_{\text{Fe-Fe}} = \frac{\mu_0}{2\chi_{\mathrm{Fe}}}(\mathbf{M}_1 \cdot \mathbf{M}_2). \quad (2)$$

To get the Rh term, we assume that the total energy is proportional to $-\mu_0 \int_0^{H_{\mathrm{eff}}} \mathbf{M}_{\mathrm{Rh}} \cdot d\mathbf{H} = -\mu_0 \chi_{\mathrm{Rh}} \int_0^{H_{\mathrm{eff}}} \mathbf{H} \cdot d\mathbf{H} = -1/2 \mu_0 \chi_{\mathrm{Rh}} H_{\mathrm{eff}}^2$:

$$W_{\mathrm{Rh}} = -\frac{\mu_0}{2}\chi_{\mathrm{Rh}}\left(\frac{\lambda}{\mu_0}(\mathbf{M}_1 + \mathbf{M}_2) + \mathbf{H}\right)^2, \quad (3)$$

where χ_{Rh} is the paramagnetic susceptibility of Rh and λ is the coupling constant between Fe and Rh spins.

The paramagnetic susceptibility χ_{Rh} of Rh, the energy of magnetic anisotropy W_{ani} and the magnetostrictive term W_{MS} deserve special attention.

B. Magnetostrictive term

To model the mutual correlations between the change in the magnetic structure and the volume changes of FeRh, we introduced in the thermodynamic potential a magnetostrictive term W_{MS}. Following Ref. [19], in the simplest approximation the energy of the Fe-Fe exchange interaction is a linear function of an applied strain u: $J(u) = J + \frac{\partial J}{\partial u}u = J + \beta u$. Hence, the part of the thermodynamic potential which depends on the strain u is

$$W_{MS} = -\beta(\mathbf{M}_1 \cdot \mathbf{M}_2)u + \frac{Eu^2}{2}, \quad (4)$$

where β is the partial derivative of the Fe-Fe exchange with respect to the strain u, and E is Young's modulus.

Minimization of the free energy with respect to the strain gives that, in thermodynamic equilibrium,

$$u = \frac{\beta}{E}\mathbf{M}_1 \cdot \mathbf{M}_2. \quad (5)$$

Substituting Eq. (5) into Eq. (4) gives

$$W_{MS} = -\frac{\beta^2}{2E}(\mathbf{M}_1 \cdot \mathbf{M}_2)^2. \quad (6)$$

C. Paramagnetic susceptibility of Rh

In our model, the temperature dependence of the paramagnetic susceptibility of Rh plays a decisive role for the phase transition between the AFM and FM states of FeRh. Interestingly, upon the phase transition from the AFM to FM state, Rh acquires a magnetic moment [16–18], and the electronic conductivity of FeRh increases by 25%–40% [11–15]. From research of electronic structure of FeRh we can outline several features: there is a charge transfer occurring between Rh and Fe in both FM and AFM phases [16], there is drastic change in the electronic structure of the valence band mostly associated with the d orbitals [30,31], while the core-level bands do not change drastically [30]. On top of that the electronic structure of iron seems to be corresponding to that in the Fe^{3+} state [30]. All these findings, in principle, suggest that the electronic structure of Rh changes upon the phase transition in FeRh as follows: Below the temperature of the phase transition, the Rh ion has an electronic configuration which does not imply a magnetic moment—$4d^{10}5s^2$—and the total angular-momentum quantum number is $J = 0$. At the phase transition Rh acquires a magnetic moment and the best candidate for the corresponding electronic structure is the $4d^9 5s^2 5p^1$ configuration with $J = 1$. Hence, while in the low-temperature AFM phase Rh contributes to the electric conductivity with its two $5s$ electrons, in the high temperature FM phase the conductivity is facilitated by an additional $5p$ electron and the expected increase in the conductivity thus amounts to about 50%. We should note, however, that the difference in 10%–25% with the theoretical prediction can be caused by the fact that the real system is distinct from the simple theoretical model, which does not account for magnetic and structural inhomogeneities and neglects that FM and AFM phases can coexist. In particular, mechanisms of spin-selective scattering can play a significant role in the inhomogeneous samples.

To model the changes in the electronic structure of Rh, we describe the latter in terms of a two-level system, as

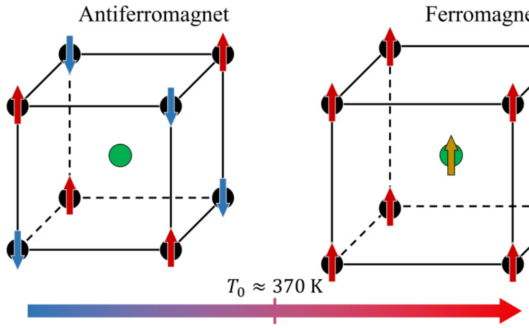

FIG. 1. First-order spin-reorientation transition in FeRh; the left picture corresponds to the antiferromagnetic phase and the right one corresponds to ferromagnetic phase. The black and green dots indicate the Fe and Rh ions respectively; red and blue (yellow) arrows schematically show the direction of the magnetic moments of the Fe (Rh) ions.

illustrated in Fig. 2. At lower temperatures all electrons occupy the nonmagnetic ground state with $J = 0$. Upon crossing the transition temperature, an electron goes to the excited state with $J = 1$. The energy difference between the ground and the excited state is denoted by Δ. We apply the Gibbs statistics to compute the magnetic susceptibility, $\chi_{\mathrm{Rh}}(T)$, modeling Rh-atom as a two-level system with the ground nonmagnetic state ($J = 0$) and excited magnetic state ($J = 1$). For a two-level system with energies ϵ_1 and ϵ_2, and an energy gap $\Delta = \epsilon_2 - \epsilon_1$, the Gibbs distribution gives the occupation probabilities $n_1(T)$ and $n_2(T)$ as

$$n_i(T) = \frac{e^{-\epsilon_i/k_BT}}{e^{-\epsilon_i/k_BT} + e^{-\epsilon_j/k_BT}}. \tag{7}$$

The total susceptibility $\chi_{\mathrm{Rh}}(T)$ can be formulated as a weighted average of the susceptibilities χ_{vv} and χ_p for the two levels:

$$\begin{aligned}\chi_{\mathrm{Rh}}(T) &= n_1(T)\chi_{\mathrm{vv}} + n_2(T)\chi_p \\ &= \frac{\chi_{\mathrm{vv}}}{1 + e^{-\Delta/k_BT}} + \frac{e^{-\Delta/k_BT}\chi_p}{1 + e^{-\Delta/k_BT}}.\end{aligned} \tag{8}$$

Here we assume that the ground level has χ_{vv} which arises due to the intermixing of the ground and excited states. And the first-excited level, being magnetic, has paramagnetic susceptibility χ_p. By employing the Gibbs statistics, we obtain a simple yet insightful expression for the temperature-dependent magnetic susceptibility of a two-level electronic system. The behavior of Rh in FeRh is very similar to the behavior of rare-earth ions, such as Eu^{3+} in Refs. [32,33], where intermixing of states gives rise to the Van Vleck susceptibility [34]. The argument for the assumed structure of the susceptibility of Rh is that Rh has a significant spin-orbit coupling due to its heavier atomic mass and higher atomic number. Spin-orbit coupling can, in principle, mix the states and thus facilitate a strong Van Vleck paramagnetism. Additionally, in a first approximation, the paramagnetic susceptibility is assumed to be constant, since $\chi_p \sim c_h(T)/k_BT$, where $c_h(T) \sim k_bT$ is the concentration of the $4d$ holes.

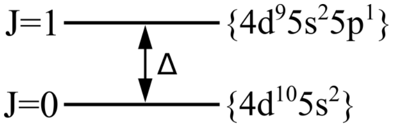

FIG. 2. Schematically represented Rh ion energy levels.

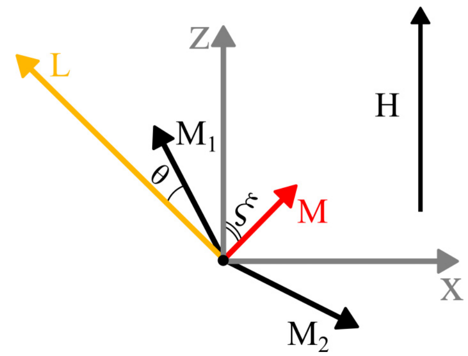

FIG. 3. Schematic coordinate system together with the vectors and corresponding angles used in the model.

D. Magnetic anisotropy

We introduce magnetic anisotropy in our model as a simple uniaxial anisotropy:

$$W_{ani} = -\tfrac{1}{2}K\left(\alpha_{\mathbf{M}_1}^2 + \alpha_{\mathbf{M}_2}^2\right), \tag{9}$$

where $\alpha_{\mathbf{M}_1}$ and $\alpha_{\mathbf{M}_2}$ are direction cosines between the anisotropy axis and $\mathbf{M}_1$, $\mathbf{M}_2$; K is the anisotropy constant. In the following, we distinguish two cases with external magnetic field along and perpendicular to the equilibrium orientation of the antiferromagnetic vector $\mathbf{L} = \mathbf{M}_1 - \mathbf{M}_2$, respectively (see Fig. 3). For the first case the direction cosines are expressed as $\alpha_{\mathbf{M}_1} = \cos(\pi/2 + \xi - \theta)$ and $\alpha_{\mathbf{M}_2} = \cos(\pi/2 - \xi - \theta)$, and for the second case the direction cosines are $\alpha_{\mathbf{M}_1} = \cos(\xi + \theta)$ and $\alpha_{\mathbf{M}_2} = \cos(\xi - \theta)$.

III. MODELLING *H*-*T* PHASE DIAGRAMS

A. Fixed and free parameters in the model

To minimize the number of free parameters in the model, we have made the following assumptions: In accordance with *ab initio* simulations from Ref. [22] we assume that the magnetic susceptibility of Fe in FeRh is $\chi_{\mathrm{Fe}} \approx 1.9 \times 10^{-3}$ and the partial derivative of the Fe-Fe exchange interaction with respect to the strain u is $\beta \approx 0.16$ T m/A. Although the Van Vleck susceptibility of the Rh ion is not known, here we rely on the similarities between the roles of Rh and Eu^{3+} for magnetic changes in FeRh and $\mathrm{Eu_2O_3}$, respectively. Hence, similarly to Eu^{3+} in Ref. [32], here we assume that $\chi_{\mathrm{vv}} \approx 1.3 \times 10^{-3}$. Young's modulus is taken from Ref. [35] as $E \approx 1.5 \times 10^{11}$ Pa. The coupling constant λ, the energy gap Δ and the paramagnetic susceptibility χ_p are fit parameters in our model Table I.

B. Estimating free parameters using fit to experimental data

To estimate the free parameters for our model, a 42-nm-thick FeRh film was grown on a MgO (001) substrate and capped with 2-nm-thick Pt layer to avoid oxidation.

TABLE I. Fixed and free parameters used in the model.

Parameter	Symbol	Value	Ref.
Magnetic susceptibility of Fe	χ_{Fe}	$\approx 1.9 \times 10^{-3}$	[22]
Partial derivatives of the Fe-Fe exchange	β	≈ 0.16 T m/A	[22]
Van Vleck susceptibility of Rh ion	χ_{vv}	$\approx 1.3 \times 10^{-3}$	[32]
Young's modulus	E	$\approx 1.5 \times 10^{11}$ Pa	[35]
Coupling constant	λ	Free	
Energy gap	Δ	Free	
Paramagnetic susceptibility	χ_p	Free	

Afterwards we patterned the as-grown sample into 50-µm-wide stripes along the [110] crystallographic direction on the MgO substrate to facilitate magnetoresistance measurements. More information on the fabrication procedure and structural characterization can be found in Refs. [36,37]. Applying an external magnetic field up to 34 T along the direction of the stripes we measured their resistance in a four-terminal configuration with a constant source-drain current of 275 nA. This detection scheme is sensitive to changes in net magnetization of the probed sample region and is seen as a change in electrical conductivity due to the magnetic phase transition. At the same time, contributions from the Hall effect and anisotropic magnetoresistance to the measured conductivity can be neglected in this geometry. The measurements were performed in the sample temperature range from 4.6 to 300 K and a few selected external magnetic field dependencies are shown in Fig. 4. In agreement with earlier reports [36,38], the resistance displays a pronounced hysteresis step as a function of the magnetic field. This can be assigned to the first-order phase transition from the (low temperature) AFM to the (high temperature) FM phase. Clearly, it is seen that the hysteresis shifts to higher magnetic fields as the temperature decreases. From these hysteresis curves we determined the critical fields of the phase transition upon an increase and decrease of the field, respectively. The corresponding values of the phase transition from AFM to FM and from FM to AFM were afterwards averaged and plotted in Fig. 5. Note that the size of the electric resistance depends on the electron-electron and electron-impurities scattering at low temperatures and electron-phonon scattering at high temperatures. As the number of phonons increases with temperature the resistance increases accordingly in correspondence with the Drude theory.

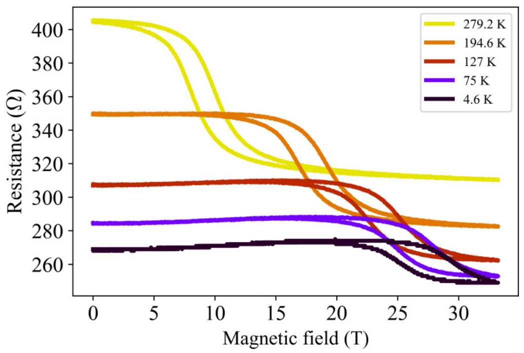

FIG. 4. Electrical resistance of a 50-µm-wide wire patterned from a 42-nm-thick FeRh film as a function of magnetic field measured at different temperatures.

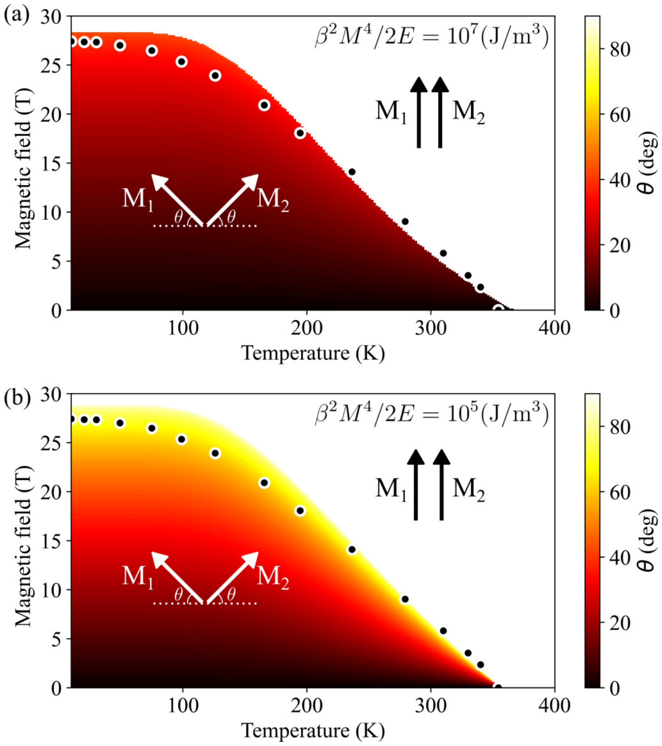

FIG. 5. Examples of H-T phase diagram along with the experimental data (black dots). Panel (a) shows the phase diagram for $\beta^2M^4/2E = 10^7$ J/m^3, $\lambda = 3.1 \times 10^{-4}$ T m/A, $\chi_p = 5.4 \times 10^{-3}$, $\Delta = 600k_b$ J. The transition from the AFM to the FM state is always of the first order. Panel (b) shows the phase diagram for $\beta^2M^4/2E = 10^5$ J/m^3, $\lambda = 3.58 \times 10^{-4}$ T m/A, $\chi_p = 3.6 \times 10^{-3}$, $\Delta = 600k_b$ J. The model predicts that the phase transition is of the first order only at zero magnetic field.

Using the model and various combinations of the free parameters, we calculated the spin arrangement corresponding to thermodynamic equilibrium at given temperatures and magnetic fields. The field in the first set of simulations is applied perpendicularly to the easy axis of magnetic anisotropy, i.e., perpendicular to the antiferromagnetic vector **L**. It appears that the ratio $\beta^2M^4/2E$, which determines the height of the barrier separating the AFM and the FM phases, is decisive for the order of the transition. In the article below, we differentiate between first- and second-order phase transitions, primarily numerically, by examining whether there is a discontinuity in magnetic order parameter (i.e., magnetization). For the cases when $\beta^2M^4/2E \gtrsim 5 \times 10^6$ J/m^3 the transition is of first order for every value of external field and temperature if the critical field does not exceed 30 T. For smaller values of $\beta^2M^4/2E$ we can get second-order phase transitions. In the first simulations we fixed the ratio $\beta^2M^4/2E = 10^7$ J/m^3, corresponding to a first-order phase transition, and fit λ, χ_p, and Δ such that the calculated critical fields agree with those observed experimentally. The resulting phase diagram shown in Fig. 5(a) was obtained for $\lambda = 3.1 \times 10^{-4}$ T m/A, $\chi_p = 5.4 \times 10^{-3}$, $\Delta = 600k_b$ J.

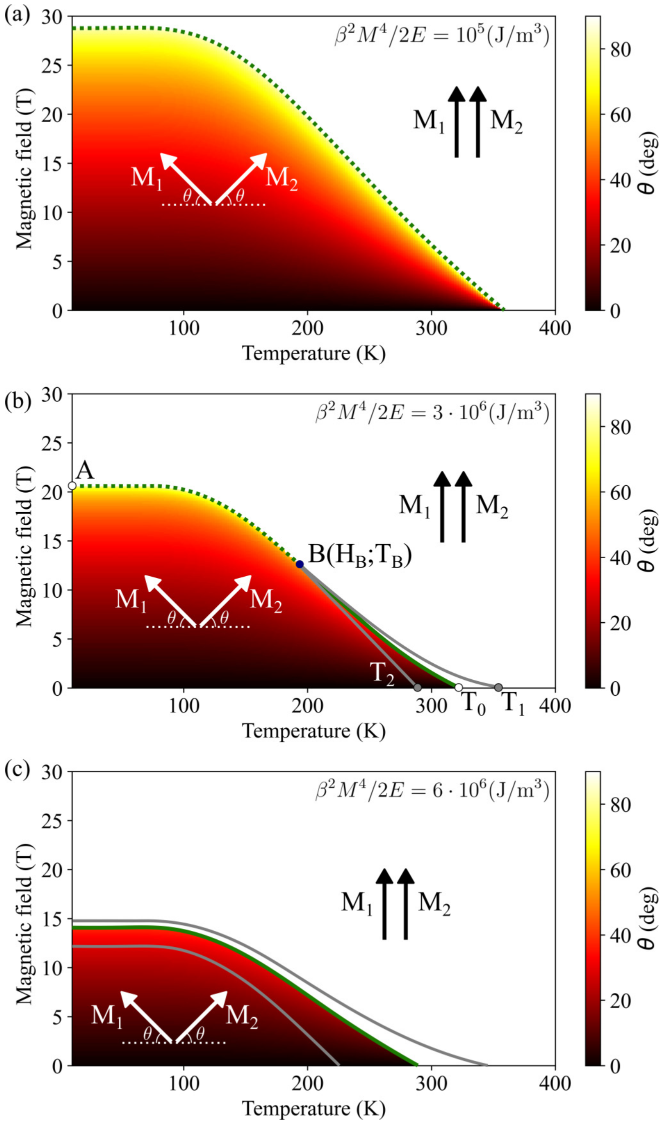

FIG. 6. Examples of H-T phase diagram (*free parameters*: $\lambda = 3.58\times10^{-4}$ T m/A, $\chi_p = 3.6\times10^{-3}$, $\Delta = 600k_b$ J) for different values of potential barrier between FM and AFM states: (a) $\beta^2M^4/2E = 10^5$ J/m^3, (b) $\beta^2M^4/2E = 3\times10^6$ J/m^3, (c) $\beta^2M^4/2E = 6\times10^6$ J/m^3. Gray solid line indicates region in which exists two minima of the thermodynamic potential, green solid line indicates a first-order phase transition, green dotted line indicates a second-order phase transition.

Furthermore, we fixed $\beta^2M^4/2E = 10^5$ J/m^3, which corresponds to a second-order phase transition, repeated the fit, and the resulting phase diagram for $\lambda = 3.58\times10^{-4}$ T m/A, $\chi_p = 3.6\times10^{-3}$, $\Delta = 600k_b$ J is shown in Fig. 5(b).

To reproduce the hysteresis behavior observed experimentally, one has to focus on the phase diagrams where the transition is of the first order and calculate lines of stability loss for FM and AFM phases. Figure 6 shows the simulated phase diagrams for various values of $\beta^2M^4/2E$. Figure 6(a) corresponds to the case of $\beta^2M^4/2E = 10^5$ J/m^3, Fig. 6(b) to $\beta^2M^4/2E = 3\times10^6$ J/m^3, Fig. 6(c) to $\beta^2M^4/2E = 6\times10^6$ J/m^3. Everywhere on the phase diagram shown in Fig. 6(a) the transition between the AFM and FM phases is of second order. Figure 6(c) shows the phase diagram for the highest $\beta^2M^4/2E$ and the transition is everywhere of first order. The intermediate value of $\beta^2M^4/2E$ results in the most complicated phase diagram with a critical point, where the transition changes the order from first to second [Fig. 6(b)]. The gray lines on the phase diagram correspond to the lines at which one of the phases, coexisting in the vicinity of the first-order phase transition, loses its stability.

From Fig. 6 we see that, for specific parameters of the model, the H-T phase diagram acquires a critical point. It is possible to analytically derive equations for lines of stability loss and, as a result, it is possible to get coordinates of the critical point. As we have no information on the Van Vleck susceptibility of Rh, here for simplicity we assume that it does not depend on the applied magnetic field. First, we find the minima of the thermodynamic potential by solving $\partial F/\partial\theta = 0$. As a result, we get two minima corresponding to the collinear FM phase: $\cos\theta = 0$ and canted AFM phase:

$$-\frac{4\chi_{\rm Fe}\beta^2M^2}{\mu_0E}\sin^3\theta+\left(1+\frac{2\chi_{\rm Fe}\beta^2M^2}{\mu_0E}-\frac{2\chi_{\rm Fe}\chi_{\rm Rh}\lambda^2}{\mu_0^2}\right)$$
$$\times\sin\theta+H\left(-\frac{\chi_{\rm Fe}}{M}-\frac{\chi_{\rm Fe}\chi_{\rm Rh}\lambda}{\mu_0M}\right)\equiv\zeta(\theta)=0.$$

These two phases can coexist. To find where each of the found phases looses its stability, we need to calculate the second derivative of the thermodynamic potential and find where it changes sign.

From $\partial^2F/\partial\theta^2 = 0$, or in an other notation $(\cos\theta)\frac{\partial\zeta}{\partial\theta} - (\sin\theta)\zeta = 0$, we first get an equation for the ABT_2 line [see Fig. 6(b)] by substituting $\cos\theta = 0$ into the expression for the second derivative:

$$\left(1-\frac{2\chi_{\rm Fe}\beta^2M^2}{\mu_0E}-\frac{2\chi_{\rm Fe}\chi_{\rm Rh}(T)\lambda^2}{\mu_0^2}\right)$$
$$+H\left(-\frac{\chi_{\rm Fe}}{M}-\frac{\chi_{\rm Fe}\chi_{\rm Rh}(T)\lambda}{\mu_0M}\right)=0. \tag{10}$$

ABT_2 corresponds to the stability loss of the collinear FM phase. Second, we can get the θ dependence for the ABT_1 line [see Fig. 6(b)] by substituting $\zeta(\theta) = 0$ into the expression for the second derivative:

$$\sin^2\theta=\frac{1}{6}\left[1-\frac{\chi_{\rm Rh}(T)E\lambda^2}{\mu_0\beta^2M^2}+\frac{\mu_0E}{2\chi_{\rm Fe}\beta^2M^2}\right]. \tag{11}$$

ABT_1 corresponds to the stability loss of the canted AFM phase. Knowing that for the temperature of the critical point $T = T_B$ we have $\sin\theta = 1$, one gets

$$\chi_{\rm Rh}(T_{\rm B})=\frac{\mu_0^2}{2\chi_{\rm Fe}\lambda^2}-\frac{5\mu_0\beta^2M^2}{E\lambda^2}. \tag{12}$$

Using Eqs. (10) and (12), one can deduce an expression for the field of the critical point H_B.

According to the experimental data shown in Fig. 4, the phase transition is characterized by a hysteresis down to 4.6 K. It suggests that the phase transition is of first order in the whole temperature range studied. Hence, the phase diagram shown in Fig. 5(a) and the corresponding set of parameters are the most suitable to fit the experimental data.

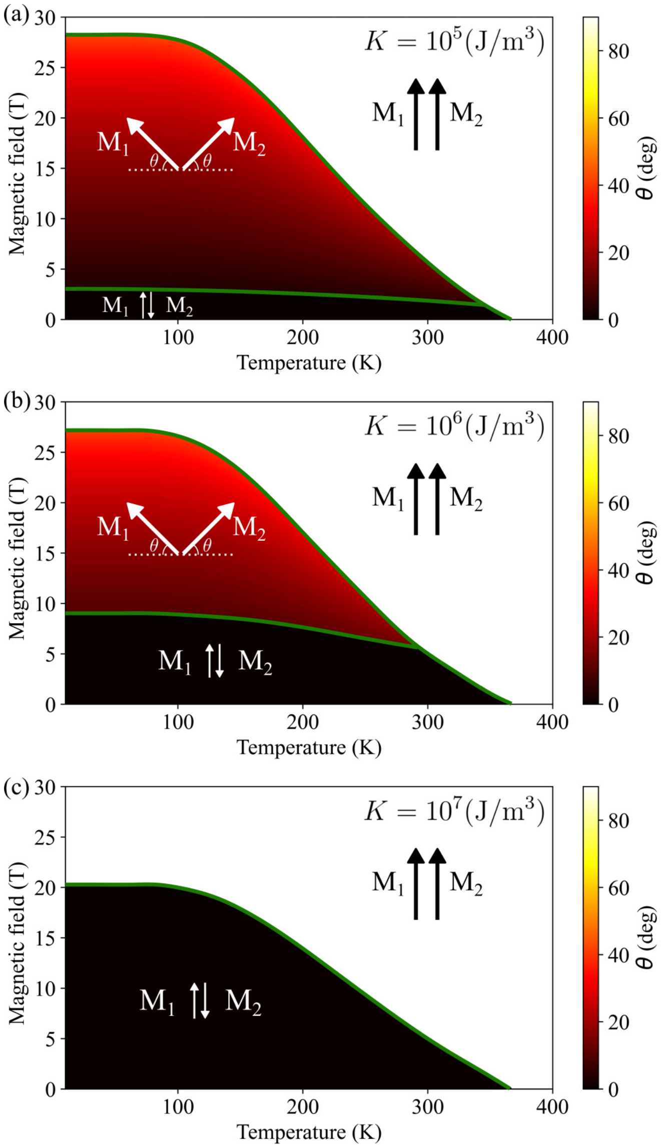

FIG. 7. Examples of H-T phase diagram (*free parameters*: $\beta^2 M^4/2E = 10^7$ J/m^3, $\lambda = 3.1 \times 10^{-4}$ T m/A, $\chi_p = 5.4 \times 10^{-3}$, $\Delta = 600 k_b$ J) with spin-flop transition: (a) $K = 10^5$ J/m^3, (b) $K = 10^6$ J/m^3, (c) $K = 10^7$ J/m^3. Green solid line indicates a first-order phase transition.

Similarly, we can calculate the H-T phase diagram for the case when the applied magnetic field is along the easy axis of magnetic anisotropy. The diagrams calculated for $\beta^2 M^4/2E = 10^7$ J/m^3, $\lambda = 3.1 \times 10^{-4}$ T m/A, $\chi_p = 5.4 \times 10^{-3}$, $\Delta = 600 k_b$ J parameters are shown in Fig. 7. In theory, it is known that, in this geometry, the spins are weakly sensitive to the external magnetic field and remain in the collinear AFM state, if the field is below the critical value $H_{\mathrm{sf}} = \sqrt{H_{ex} H_A}$, where H_{ex} and H_A are the effective fields of the Fe-Fe exchange interaction and magnetic anisotropy, respectively. At the critical field H_{sf}, the spin structure experiences a so-called spin-flop transition, where the spins rotate over nearly 90° and get slightly canted, thus forming a canted AFM phase. Hence, the strength of the magnetic anisotropy starts to play a significant role. Here we model how the phase diagram changes for different values of the anisotropy constant K. It is seen that, unlike the diagrams shown in Fig. 6, application of a magnetic field along the antiferromagnetic vector results in three different phases: collinear AFM, noncollinear AFM, and FM. From the diagrams shown in Fig. 7 it is seen that the larger the magnetic anisotropy, the narrower the region of magnetic fields that correspond to the canted AFM phase. Eventually, if the magnetic anisotropy is large enough, no canted AFM phase is observed. We should note, however, that the effective field for such a strong magnetic anisotropy would be comparable with the effective field of the exchange interaction and thus very exotic, if not unrealistic. Nonetheless, in the case of FeRh it may be possible in the AFM phase, where the coupling between Fe and Rh spins significantly reduces the effective Fe-Fe exchange interaction. We found that the phase transition from the canted AFM to FM state on these phase diagrams is always of first order. Hence, all the diagrams agree well with the hysteresis behavior observed experimentally in the magnetoresistance measurements (see Fig. 4). Hence the diagrams shown in Fig. 5(a) and Fig. 7 can all fit the experimental observations.

IV. X-RAY ABSORPTION NEAR-EDGE SPECTRA, X-RAY MAGNETIC CIRCULAR DICHROISM MEASUREMENTS AND DISCUSSION

The x-ray-absorption near-edge structure (XANES) and x-ray magnetic circular dichroism (XMCD) spectra of the 42-nm-thick FeRh film, at the Rh $L_{2,3}$ and Fe K absorption edges, were measured at the European Synchrotron Radiation Facility (ESRF) beamline ID12 (see Fig. 8). The first harmonic of the helical undulator was used to provide circularly polarized x-rays in the energy range between 3.0 and 3.2 keV and between 7.1 and 7.2 keV. At these energies, the Bragg angle of the Si[111] double-crystal monochromator is close to the Brewster angle of 45°. This leads to a strong reduction of the circular polarization rate of the x-ray beam, down to 12% and 5% at the L_2 and L_3 edges of Rh, respectively. The XANES spectra were recorded in the total fluorescence yield detection mode, using Si photodiodes. The XMCD spectra were obtained as the direct difference of the XANES spectra recorded with the helicity either antiparallel or parallel to the magnetic field applied to the sample. To eliminate possible experimental artifacts, the XMCD spectra were measured for two opposite directions of the applied magnetic field. The spectra were corrected for the incomplete circular polarization rate. The XMCD was measured at magnetic fields up to 17 T produced by a superconducting solenoid. To derive the spin and orbital moments carried by the Rh 4d electrons, the magneto-optical sum rules were applied to the experimental XMCD spectra [39,40]:

$$\begin{aligned} M_L &= (-2/3)(A_3 + A_2) n_{4d}/\sigma_{\mathrm{tot}}, \\ M_S &= -(A_3 - 2A_2) n_{4d}/\sigma_{\mathrm{tot}}, \end{aligned} \tag{13}$$

where A_2 and A_3 are the integrated XMCD signals at the L_2 and L_3 edges, respectively, n_{4d} is the number of holes in the Rh 4d bands, σ_{tot} is the total absorption cross section corresponding to 2p-4d transitions. Following the standard procedure [41,42], the normalized x-ray absorption cross section per 4d hole, $n_{4d}/\sigma_{\mathrm{tot}} = 0.144$, was determined by subtracting the Ag-foil $L_{2,3}$ spectra from the experimental Rh $L_{2,3}$

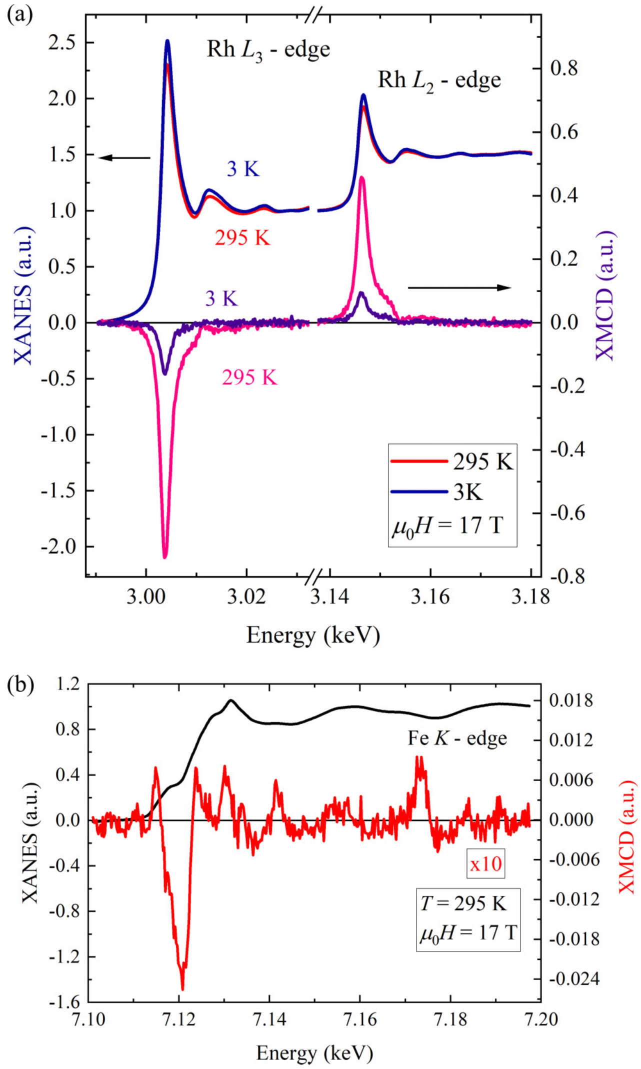

FIG. 8. Example spectra of XANES and XMCD for temperatures of 3 K, 295 K, and external field of 17 T for: (a) Rh $L_{2,3}$ edges, (b) Fe K edge.

spectra measured on the FeRh film and taking the theoretical value for the number of Rh 4d holes (2.34) from Ref. [43]. Using this value, the Rh 4d spin and orbital magnetic moments were derived (Fig. 9 and inset of Fig. 9). Pure Rh ions are paramagnetic and also acquire a moment in an external magnetic field. For 3 K and 17 T, the spin moment due to Pauli paramagnetism cannot exceed $0.0027\mu_B$ [44], which is almost two orders of magnitude lower in comparison with the obtained $0.19\mu_B$. However, it could not be referred to the ferromagnetism of Rh, observed in clusters ($0.067\mu_B$) [45]. Thus, we suggest that this moment reflects the canting of the Fe magnetization in a high magnetic field. Latter in the text we use XMCD measurements on Rh sites but not on Fe sites because signal strengths are higher and, on top of that, the hysteresis behavior on Rh and Fe sites coincides (see Fig. 10).

Figure 11 shows the XMCD curves as a function of the magnetic field at different temperatures, defined as follows:

$$\Delta\mathrm{XMCD} = \frac{1}{2A}[A_+(r) - A_+(l)] + [A_-(r) - A_-(l)], \quad (14)$$

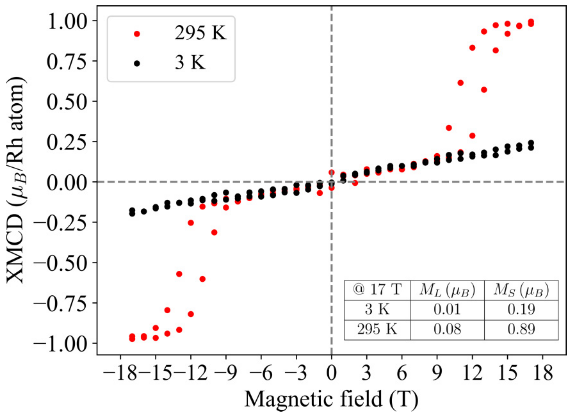

@ 17 T	$M_L\,(\mu_B)$	$M_S\,(\mu_B)$
3 K	0.01	0.19
295 K	0.08	0.89

FIG. 9. Magnetic moment of Rh ion as a function of external field for two different temperatures 3 and 295 K derived directly from XMCD measurements. XMCD data (originally in arbitrary units) were normalized to the $M_{\mathrm{tot}} = M_S + M_L$ values calculated based on the sum rules at 3 and 295 K and 17 T.

where A is the average absorption at the energy of 3.0037 keV, corresponding to the maximum of the XMCD spectra at the Rh L_3 edge. A_+ and A_- are the absorption at a positive and a negative external magnetic field, respectively. $A(r)$ and $A(l)$ are absorptions of left- and right-circular x-ray polarization. Thus, ΔXMCD reflects the maximal magnetic circular dichroism relative to the total absorption at the considered Rh edge. Figure 11 shows the experimentally obtained field dependencies of the ΔXMCD signal, which mimics the values of the magnetic moments of Rh per valence hole induced by an effective field on the Rh sites. The experiments reveal that at fields below those at which the hysteresis opens up (<10 T), one can clearly distinguish slopes in the ΔXMCD signal as a function of magnetic field. The slope corresponds to spins canting over angles no more than 10°. At 325 K, no slope is observed for fields above the hysteresis, implying that the spins are completely aligned and further increase of the field does not result in an increase of the magnetization. To compare the experimental results with the simulated phase diagrams, on the same graph we plot the numerically calculated field sweeps. Taking the diagram from Fig. 5(a)

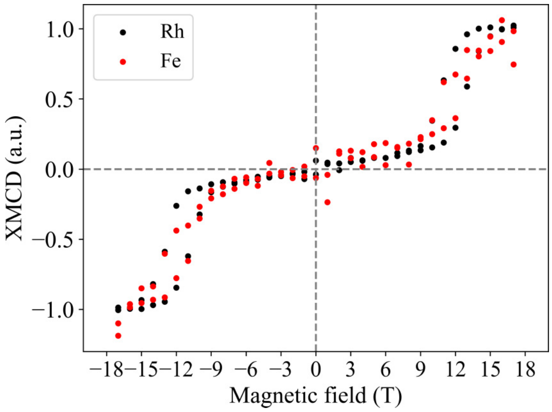

FIG. 10. XMCD measurements in a.u. for Fe and Rh ions as a function of external field at a temperature of 295 K.

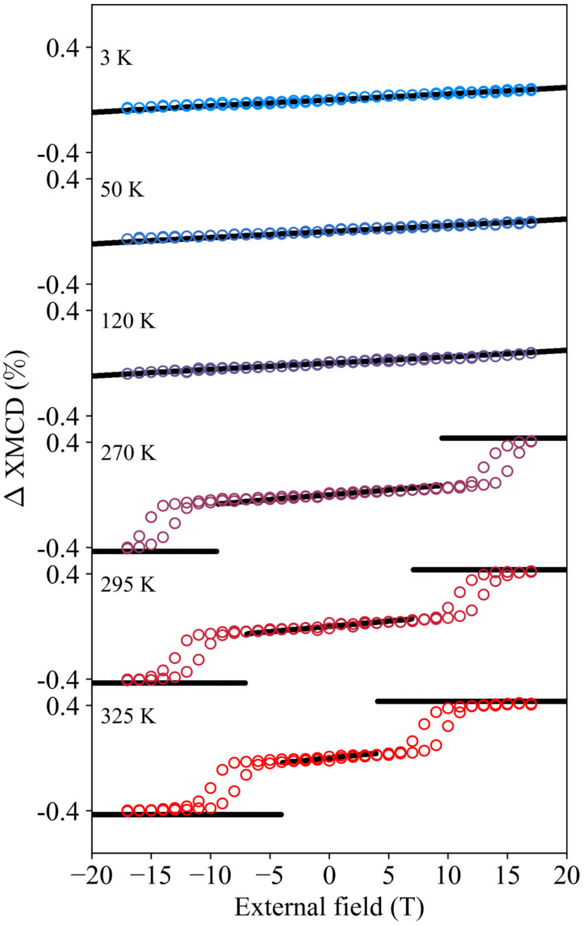

FIG. 11. ΔXMCD as a function of the magnetic field at different temperatures. Filled black dots are Δ XMCD from theory for $\beta^2 M^4/2E = 3 \times 10^7$ J/m^3, $\lambda = 2.3 \times 10^{-4}$ T m/A, $\chi_p = 9.4 \times 10^{-3}$, $\Delta = 600 k_b$ J; unfilled dots are ΔXMCD measurements.

as an initial guess, we slightly tuned the parameters in order to fit the experimental data: $\beta^2 M^4/2E = 3 \times 10^7$ J/m^3, $\lambda = 2.3 \times 10^{-4}$ T m/A, $\chi_p = 9.4 \times 10^{-3}$, $\Delta = 600 k_b$ J. It is seen that the calculated sweeps fit well to those observed experimentally. This agreement is not unique, however. If the field is applied parallel to the easy axis of magnetic anisotropy, as for the case of the H-T phase diagrams shown in Fig. 7(a), the calculated sweeps appear to be very similar. For instance, for the case of $K = 10^5$ J/m^3 the obtained field dependencies are very identical to those for the case, when the field is applied perpendicularly to the easy axis. Again, in the fields below 10 T the spin canting does not exceed 10°. Implying that the comparison of the experimental and calculated dependencies does not allow us to identify the type of magnetic anisotropy of FeRh-films in the AFM state. Nevertheless, as the experimentally observed spin canting in the fields below 10 T is not zero, we can conclude that the anisotropy in the real FeRh films is not high enough to suppress a spin-canted state. Indeed, the case would correspond to the phase diagram shown in Fig. 7(c). In this case, the applied magnetic field is unable to tilt the spins up to the values of the spin-flop field. Meaning that the phase diagram shown in Fig. 7(c) can be excluded. Hence, we have managed to limit the number of the most suitable phase diagrams for FeRh. In particular, the diagrams shown in Figs. 5(a) and 7(a) do fit the experimental data in the best way.

V. CONCLUSIONS

Using the approach of mean-field theory, we studied H-T phase diagrams of the magneto-structural phase transition in FeRh. Varying parameters in the theory we suggest a number of H-T phase diagrams. Analyzing the experimental electrical resistance in magnetic field data, we reveal that the field induced phase transition is of first order in a broad range of temperatures. This fact, together with the values of the magnetic fields at which the transition occurs, allows us to narrow down the set of the suitable phase diagrams and the range of corresponding parameters. Measuring XMCD and XANES at the Rh and Fe edges, we revealed the field dependencies of the magnetic moment of Rh, which is a signature of the phase transition and of the noncollinear AFM phase which is present in an external magnetic field before the AFM-to-FM phase transition in FeRh. Unfortunately, the comparison of the experimental data and the calculated phase diagrams did not allow us to identify the magnetic anisotropy of FeRh in the AFM phase. Although we can conclude that the anisotropy is not high enough to suppress a spin-canted phase, the strength of the magnetic anisotropy and the orientation of its easy axis remain subjects for future studies.

ACKNOWLEDGMENTS

The authors would like to thank A. Rogalev for his help with the XANES and XMCD measurements and useful discussions. The project has received funding from the European Union’s Horizon 2020 research and innovation programme under the Marie Skłodowska-Curie Grant Agreement No. 861300 (COMRAD) and the European Research Council ERC Grant Agreement No. 856538 (3D-MAGiC). S.K.K.P., R.M., and E.E.F. acknowledge support from the National Science Foundation, Division of Materials Research (Award No: 2105400). High field transport measurements were conducted as part of a user project supported by the High Field Magnet Laboratory and the Foundation for Dutch Scientific Research Institutes (HFML-RU/NWO-I), member of the European Magnetic Field Laboratory (EMFL). A.K.Z. acknowledges financial support by the Russian Science Foundation, Project No. 22-12-00367. The authors declare that this work has been published as a result of peer-to-peer scientific collaboration between researchers. The provided affiliations represent the actual addresses of the authors in agreement with their digital identifier (ORCID) and cannot be considered as a formal collaboration between the aforementioned institutions.

[1] L. D. Landau, Possible explanation of the dependence on the field of the susceptibility at low temperatures, Phys. Z. Sowjet. **4**, 675 (1933).

[2] M. L. Néel, Propriétés magnétiques des ferrites; ferrimagnétisme et antiferromagnétisme, Ann. Phys. (Paris, Fr.) **12**, 137 (1948).

[3] T. Jungwirth, X. Marti, P. Wadley, and J. Wunderlich, Antiferromagnetic spintronics, Nat. Nanotechnol. **11**, 231 (2016).

[4] C. Song, Y. You, X. Chen, X. Zhou, Y. Wang, and F. Pan, How to manipulate magnetic states of antiferromagnets, Nanotechnol. **29**, 112001 (2018).

[5] A. Barman, G. Gubbiotti, S. Ladak, A. O. Adeyeye, M. Krawczyk, J. Gräfe, C. Adelmann, S. Cotofana, A. Naeemi, V. I. Vasyuchka *et al.*, The 2021 magnonics roadmap, J. Phys.: Condens. Matter **33**, 413001 (2021).

[6] V. Baltz, A. Manchon, M. Tsoi, T. Moriyama, T. Ono, and Y. Tserkovnyak, Antiferromagnetic spintronics, Rev. Mod. Phys. **90**, 015005 (2018).

[7] L. Šmejkal, J. Sinova, and T. Jungwirth, Emerging research landscape of altermagnetism, Phys. Rev. X **12**, 040501 (2022).

[8] M. Fallot, Les alliages du fer avec les métaux de la famille du platine, Ann. Phys. (Paris, Fr.) **11**, 291 (1938).

[9] L. Zsoldos, Lattice parameter change of FeRh alloys due to antiferromagnetic-ferromagnetic transformation, Phys. Status Solidi B **20**, K25 (1967).

[10] A. I. Zakharov, A. M. Kadomtseva, R. Z. Levitin, and E. G. Ponyatovskii, Magnetic and magnetoelastic properties of a metamagnetic iron-rhodium alloy, Sov. Phys. JETP **19**, 1348 (1964).

[11] J. S. Kouvel and C. C. Hartelius, Anomalous magnetic moments and transformations in the ordered alloy FeRh, J. Appl. Phys. **33**, 1343 (1962).

[12] J. M. Lommel, Magnetic and electrical properties of FeRh thin films, J. Appl. Phys. **37**, 1483 (1966).

[13] C. J. Schinkel, R. Hartog, and F. H. Hochstenbach, On the magnetic and electrical properties of nearly equiatomic ordered FeRh alloys, J. Phys. F: Met. Phys. **4**, 1412 (1974).

[14] L. H. Lewis, C. H. Marrows, and S. Langridge, Coupled magnetic, structural, and electronic phase transitions in FeRh, J. Phys. D: Appl. Phys. **49**, 323002 (2016).

[15] N. A. Blumenschein, G. M. Stephen, C. D. Cress, S. W. LaGasse, A. T. Hanbicki, S. P. Bennett, and A. L. Friedman, High-speed metamagnetic switching of FeRh through joule heating, Sci. Rep. **12**, 22061(2022).

[16] V. L. Moruzzi and P. M. Marcus, Antiferromagnetic-ferromagnetic transition in FeRh, Phys. Rev. B **46**, 2864 (1992).

[17] G. Shirane, C. W. Chen, P. A. Flinn, and R. Nathans, Hyperfine fields and magnetic moments in the Fe-Rh system, J. Appl. Phys. **34**, 1044 (1963).

[18] G. Shirane, R. Nathans, and C. W. Chen, Magnetic moments and unpaired spin densities in the Fe-Rh alloys, Phys. Rev. **134**, A1547(1964).

[19] C. Kittel, Model of exchange-inversion magnetization, Phys. Rev. **120**, 335 (1960).

[20] J. S. Kouvel, Unusual nature of the abrupt magnetic transition in FeRh and its pseudobinary variants, J. Appl. Phys. **37**, 1257 (1966).

[21] J. B. Mckinnon, D. Melville, and E. W. Lee, The antiferromagnetic-ferromagnetic transition in iron-rhodium alloys, J. Phys. C: Solid State Phys. **3**, S46 (1970).

[22] M. E. Gruner, E. Hoffmann, and P. Entel, Instability of the rhodium magnetic moment as the origin of the metamagnetic phase transition in α—FeRh, Phys. Rev. B **67**, 064415 (2003).

[23] G. Ju, J. Hohlfeld, B. Bergman, R. J. M. van de Veerdonk, O. N. Mryasov, J.-Y. Kim, X. Wu, D. Weller, and B. Koopmans, Ultrafast generation of ferromagnetic order via a laser-induced phase transformation in FeRh thin films, Phys. Rev. Lett. **93**, 197403 (2004).

[24] R. Y. Gu and V. P. Antropov, Dominance of the spin-wave contribution to the magnetic phase transition in FeRh, Phys. Rev. B **72**, 012403 (2005).

[25] L. M. Sandratskii and P. Mavropoulos, Magnetic excitations and femtomagnetism of FeRh: A first-principles study, Phys. Rev. B **83**, 174408 (2011).

[26] O. N. Mryasov, Magnetic interactions and phase transformations in FeM, M = (Pt, Rh) ordered alloys, Phase Trans. **78**, 197 (2005).

[27] J. Barker and R. W. Chantrell, Higher-order exchange interactions leading to metamagnetism in FeRh, Phys. Rev. B **92**, 094402 (2015).

[28] M. P. Belov, A. B. Syzdykova, and I. A. Abrikosov, Temperature-dependent lattice dynamics of antiferromagnetic and ferromagnetic phases of FeRh, Phys. Rev. B **101**, 134303 (2020).

[29] A. Botterman, Ph.D. thesis, Eindhoven University of Technology, 1976.

[30] A. X. Gray, D. W. Cooke, P. Krüger, C. Bordel, A. M. Kaiser, S. Moyerman, E. E. Fullerton, S. Ueda, Y. Yamashita, A. Gloskovskii *et al.*, Electronic structure changes across the metamagnetic transition in FeRh via hard x-ray photoemission, Phys. Rev. Lett. **108**, 257208 (2012).

[31] H. Takahashi, M. Araidai, S. Okada, and K. Shiraishi, Theoretical investigation on electronic and magnetic structures of FeRh, J. Magn. Soc. Jpn. **40**, 77 (2016).

[32] Y. Takikawa, S. Ebisu, and S. Nagata, Van Vleck paramagnetism of the trivalent Eu ions, J. Phys. Chem. Solids **71**, 1592 (2010).

[33] H. Samata, N. Wada, and T. C. Ozawa, Van Vleck paramagnetism of europium oxyhydroxide, J. Rare Earths **33**, 177 (2015).

[34] J. H. Van Vleck and A. Frank, The effect of second order Zeeman terms on magnetic susceptibilities in the rare earth and iron groups, Phys. Rev. **34**, 1494 (1929).

[35] W. He, H. Huang, and X. Ma, First-principles calculations on elastic and entropy properties in FeRh alloys, Mater. Lett. **195**, 156 (2017).

[36] V. Uhlíř, J. A. Arregi, and E. E. Fullerton, Colossal magnetic phase transition asymmetry in mesoscale FeRh stripes, Nat. Commun. **7**, 13113 (2016).

[37] G. Li, R. Medapalli, J. H. Mentink, R. V. Mikhaylovskiy, T. G. Blank, S. K. Patel, A. K. Zvezdin, T. Rasing, E. E. Fullerton, and A. V. Kimel, Ultrafast kinetics of the antiferromagnetic-ferromagnetic phase transition in FeRh, Nat. Commun. **13**, 2998 (2022).

[38] S. Maat, J.-U. Thiele, and E. E. Fullerton, Temperature and field hysteresis of the antiferromagnetic-to-ferromagnetic phase transition in epitaxial FeRh films, Phys. Rev. B **72**, 214432 (2005).

[39] B. T. Thole, P. Carra, F. Sette, and G. van der Laan, X-ray circular dichroism as a probe of orbital magnetization, Phys. Rev. Lett. **68**, 1943 (1992).

[40] P. Carra, B. T. Thole, M. Altarelli, and X. Wang, X-ray circular dichroism and local magnetic fields, Phys. Rev. Lett. **70**, 694 (1993).

[41] V. M. T. S. Barthem, A. Rogalev, F. Wilhelm, M. M. Sant'Anna, S. L. A. Mello, Y. Zhang, P. Bayle-Guillemaud, and D. Givord, Spin fluctuations of paramagnetic Rh clusters revealed by x-ray magnetic circular dichroism, Phys. Rev. Lett. **109**, 197204 (2012).

[42] J. Vogel, A. Fontaine, V. Cros, F. Petroff, J.-P. Kappler, G. Krill, A. Rogalev, and J. Goulon, Palladium magnetism in Pd/Fe multilayers studied by XMCD at the Pd$L_{2,3}$ edges, J. Magn. Magn. Mater. **165**, 96 (1997).

[43] C. Stamm, J.-U. Thiele, T. Kachel, I. Radu, P. Ramm, M. Kosuth, J. Minár, H. Ebert, H. A. Dürr, W. Eberhardt *et al.*, Antiferromagnetic-ferromagnetic phase transition in FeRh probed by x-ray magnetic circular dichroism, Phys. Rev. B **77**, 184401 (2008).

[44] F. E. Hoare and J. C. Walling, An absolute measurement of the susceptibility of tantalum and other metals, Proc. Phys. Soc., London, Sect. B **64**, 337 (1951).

[45] A. Rogalev and F. Wilhelm, Magnetic circular dichroism in the hard x-ray range, Phys. Metals Metallogr. **116**, 1285 (2015).